Acta Materialia 202 (2021) 350–365

Contents lists available at ScienceDirect

Acta Materialia

journal homepage: www.elsevier.com/locate/actamat

Fracture mechanism and toughness of a rolled magnesium alloy under dynamic loading

Arjun Sreedhar S[a], Suraj Ravindran[b], Gyan Shankar[c], S. Suwas[c], R. Narasimhan[a,*]

[a] Department of Mechanical Engineering, Indian Institute of Science, Bangalore 560012, India
[b] Graduate Aeronautical Laboratories, California Institute of Technology, Pasadena, California 91125, USA
[c] Department of Materials Engineering, Indian Institute of Science, Bangalore 560012, India

ARTICLE INFO

Article history:
Received 8 June 2020
Revised 14 October 2020
Accepted 26 October 2020
Available online 2 November 2020

Keywords:
Dynamic fracture initiation
Rolled Mg alloy
Texture
Tensile twinning
Crack tip constraint
Fracture toughness

ABSTRACT

Static and dynamic fracture experiments are performed using fatigue pre-cracked three-point bend specimens of a rolled AZ31 Mg alloy on a servo-hydraulic universal testing machine and a Hopkinson bar setup, respectively. The results are interpreted using in-situ optical imaging along with digital image correlation analysis. Microstructural analysis reveals that the fracture mechanism changes from twin-induced quasi-brittle cracking for static loading to micro-void growth and coalescence under dynamic loading accompanied by decrease in tensile twinning near the tip with loading rate. By contrast, the density of twins near the far-edge of the ligament and associated texture change enhance strongly with loading rate. The fracture toughness increases dramatically at high loading rates which is attributed to enhanced work of separation and dissipation in the background plastic zone.

1. Introduction

The mechanical and fracture behavior of magnesium alloys are currently the focus of considerable research work due to their attractive properties, such as low density, high specific strength and good machinability. However, they have poor corrosion resistance as well as lower fracture toughness than Al alloys which has hindered their utilization [1–4]. Magnesium has HCP crystal structure and plastically deforms at room temperature by slip, as well as by $\{10\bar{1}2\}$ and $\{10\bar{1}1\}$ twins [4–6].These are referred to as tensile and contraction twins (TTs, CTs), respectively (because they cause extension and contraction along c-axis). The vastly differing critical resolved shear stress (CRSS) values of various slip and twin systems and strong textures make Mg alloys inherently anisotropic [3,5].

The orientation dependent stress-strain behaviours of wrought Mg alloys under uniaxial tension and compression at different strain rates and temperatures have been studied extensively [7–10]. Ulacia et al. [8] and Dudamell et al. [9] observed that the yield stress remains almost constant for all compression tests (up to strain rate of 10^3 s^{-1}), whereas for tension along rolling direction (RD) it increases. However, Zhao et al. [10] reported that, while rate dependence during compression along rolling, transverse and normal directions (RD, TD and ND) for AZ31B Mg alloy is negligible up to strain rate of 10^3 s^{-1}, a strong elevation of flow stress and strain to failure occurs above strain rates of the order 10^4 s^{-1}. An increase in TT activity was also observed with strain rate for Mg alloys, especially under RD/TD compression [8,9].

The fracture behaviour of Mg alloys under static loading has been extensively investigated [2,11–22]. Somekawa et al. [2,11,12] observed an increase in K_{IC} and decrease in tensile twinning as grain size is refined, along with a change in fracture mechanism from twin-induced crack propagation to ductile void growth and coalescence. Kaushik et al. [13] conducted static experiments on notched three-point bend fracture specimens of Mg single crystals. They noted a direct correlation between evolution histories of TT volume fraction and energy release rate J even though crack extension took place along twin boundaries. In contrast to [12], Prasad et al. [14] reported that fibrous failure occurs for a rolled AZ31 Mg alloy from experiments performed with notched compact tension specimens. They noted that a significant contribution to toughness (roughly 70%) arises from profuse tensile twinning in the background plastic zone which corroborates with [13]. Further, a strong enhancement in J_c with notch size was also noticed in [15] accompanied by a brittle-ductile transition. The complex interplay between stress triaxiality level (varied by changing the notch size) and plastic anisotropy has been found to influence ductility and failure mechanism in notched cylindrical AZ31 Mg alloy bars under tensile loading [3]. Moreover, crystal plasticity finite element

* Corresponding author.
E-mail address: narasi@iisc.ac.in (R. Narasimhan).

https://doi.org/10.1016/j.actamat.2020.10.059
1359-6454/

(CPFE) simulations [16,17] have revealed that high stress triaxiality near sharp notches can activate TTs, which in turn, promote brittle fracture.

In automotive and aerospace applications, rapid loading of structural components may occur owing to crash or impact. Under such conditions, dynamic fracture initiation of pre-existing fatigue cracks at stress concentrations like cut-outs and rivet holes becomes important [23]. Therefore, since Mg alloys are envisaged for such applications [1], it is imperative to investigate their dynamic fracture behavior. Experimental studies carried out on various steels and Al alloys [24–28] have shown that the fracture toughness enhances with loading rate, if ductile fracture takes place. On the contrary, it may decrease with loading rate if cleavage fracture mechanism is dominant [24,25]. In order to rationalize the above observed trends of dynamic fracture toughness with loading rate, the stress fields near a dynamically loaded crack tip in isotropic elastic-plastic solids as well as FCC single crystals have been systematically investigated [29–33]. These studies have shown that as loading rate increases, even high constraint geometries like deeply cracked three-point bend specimens will experience progressive loss of constraint (or triaxiality). In other words, the constraint parameter Q [34,35] becomes more negative as $\dot{J}$ increases. Jayadevan et al. [31] and Biswas and Narasimhan [30] have applied the above inertia-driven constraint loss to explain the enhancement in toughness with loading rate in nearly rate independent plastic solids. In [30,36], it was observed that material inertia and strain rate sensitivity retard void growth near a crack tip and enhance the ductile fracture toughness.

In contrast to steels and Al alloys, very few investigations have been conducted on dynamic fracture response of Mg alloys. Yu et al. [37] performed dynamic fracture experiments, coupled with finite element analysis, on AZ31B Mg alloy and found an increasing trend in fracture toughness K_c with loading rate. Daud et al. [38] conducted dynamic fracture experiments on fatigue pre-cracked three-point bend AZ61 Mg alloy specimens of varying thickness using Charpy impact testing machine and noted a decrease in toughness with specimen thickness.

However, a comprehensive study on effect of loading rate on fracture behaviour of Mg alloys needs to be performed to address the following important issues.

- How does the loading rate influence the operative fracture mechanism? Does this mechanism change with increase in loading rate akin to the effect of notch root radius in static experiments, since triaxiality will be similarly affected by both these factors as mentioned above?
- What is the effect of loading rate on the TT development near the crack tip as well as over the entire uncracked ligament? Does this cause strong changes in the crystallographic texture?
- How does the strain distribution in the ligament (both near the tip and away from it) change as the loading rate enhances? Can this be correlated with the TT activity and texture changes?
- What is the influence of loading rate on the dynamic crack initiation toughness, J_c? Can this trend be rationalized from the role of tensile twinning in influencing the observed fracture mechanism and background plastic dissipation?

In order to answer the above questions, static and dynamic three-point bend fracture experiments are conducted on a rolled (basal-textured) AZ31 Mg alloy using an universal testing machine (UTM) and Hopkinson pressure bar, respectively. In-situ optical imaging along with digital image correlation (DIC) analysis is performed to extract the displacement and strain fields. Also, microstructural investigations including optical microscopy, fractography and electron back scattered diffraction (EBSD) are carried out on the fractured samples to get key insights on TT development, texture changes and operative fracture mechanism. An important aspect of the present work is that the displacement and strain data obtained from DIC maps are used along with the procedure suggested by Nakamura et al. [39] to compute the time history of J. This obviates recourse to complementary finite element analysis or using handbook formula, as in [37,38]. The results show a strong enhancement in fracture toughness, J_c, along with a change in fracture mechanism from twinning-induced quasi-brittle fracture to ductile void growth and coalescence as loading rate enhances. The intensity of twinning near the loading-end of the ligament and associated texture change enhance strongly with impact velocity. Thus, tensile twinning plays a dual role on dynamic fracture of Mg alloys. It affects near-tip fracture processes (which can be detrimental) and the plastic work expended in the ligament (which is beneficial).

2. Materials and methods

2.1. Material and specimen preparation

Single edge notched specimens are machined using wire-cut electric discharge machining (EDM) from an as-received 12.7 mm thick rolled AZ31 Mg alloy plate. The chemical composition by weight percentage of this alloy is presented in Table 1. Fig. 1 shows a schematic of a specimen which has a length $L = 90$ mm, width, $W = 20$ mm and thickness, $B = 6.3$ mm. The specimens are machined such that RD is along its length and TD is along its width. Earlier studies [14,20] have shown that fracture specimens tested under quasi-static loading with the crack along RD and TD display negligible differences in response. A starter notch of diameter about 350 μm is first cut along the width using EDM to a length of 9.3 mm. It is then subjected to fatigue loading under four-point bend configuration with a small load amplitude of 1.4 kN in an UTM, INSTRON 8502, at a frequency of 3 Hz till a crack length of about 0.7 mm grows from the starter notch. Thus, the effective crack length to width ratio of the specimen $a/W = 0.5$.

Optical metallography and EBSD after pre-cracking are carried out following the procedure explained in Section 2.3 to examine the initial microstructure of the alloy and to ascertain if any twinning has occurred during the specimen preparation. Fig. 2(a) shows an optical micrograph while Figs. 2(b) and (c) display the inverse pole figure (IPF) map and (0001) / (11$\bar{2}$0) pole figures (PFs), respectively, near the fatigue pre-crack tip. A bimodal grain size distribution can be observed with an average grain size of 10.6 ± 5 μm which was estimated by the area fraction method. Also, it can be seen from Figs. 2(b) and (c) that the texture is near-basal. Figs. 2(a) and (b) confirm that no twinning has been induced during specimen preparation, especially near the fatigue pre-crack tip.

Table 1
Composition of AZ31 Mg alloy by weight%.

Element	Mg	Al	Zn	Mn
Weight%	95.88	2.75	1.12	0.14

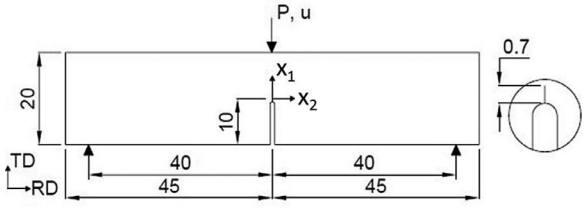

Fig. 1. Schematic of the specimen employed in both the static and dynamic tests along with a detailed view of the initial pre-crack tip that is grown by fatigue loading from an EDM-cut notch. All dimensions are in mm.

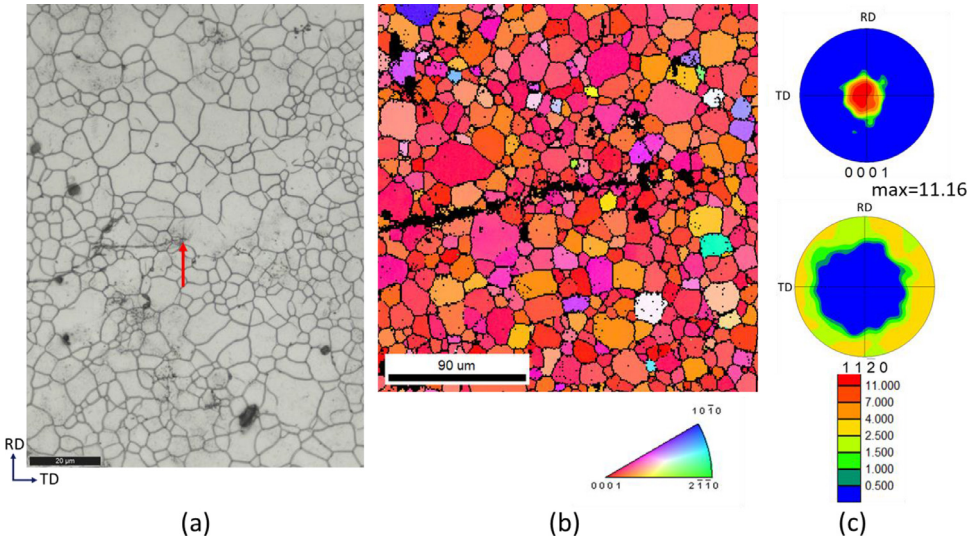

Fig. 2. (a) Optical micrograph near fatigue pre-crack tip (which is indicated by the red vertical arrow), (b) IPF map near the fatigue pre-crack tip and (c) corresponding (0001) and ($11\bar{2}0$) pole figures. (For interpretation of the references to colour in this figure legend, the reader is referred to the web version of this article.)

2.2. Experimental procedure

2.2.1. Static fracture test

Static, mode I fracture test is carried out under three-point bend configuration using the above specimen (Fig. 1) with a span of 80 mm and over-hangs of 5 mm at either end on the UTM, with custom-made grips. A displacement rate of 0.001 mm/*sec* is applied in this experiment which is performed three times to obtain repeatable results. In addition to the load and actuator displacement, images of the deformed specimen are captured at regular intervals with a digital camera, Nikon D7000, having a resolution of 16.9 megapixels. A speckle pattern of very fine black dots over a white background is applied on the specimen surface using acrylic paint with the help of an air-brush. The displacement and strain fields are subsequently obtained by analyzing these images using Vic-2D DIC software to obtain the displacement and strain fields.

The specimen rotation, θ, about the hinge point, located ahead of the crack tip on the ligament is ascertained from the crack mouth opening displacement δ_{m}, determined from DIC analysis, as

$$\theta = \frac{\delta_m}{(a + rb)} \ . \tag{1}$$

In the above equation, r ($0 < r < 1$) is a factor that gives the location of the hinge point, which is inferred from normal strain variation on the ligament as about 0.4. The specimen rotation θ, is divided into elastic and plastic parts, θ_{e} and θ_{p}. The plastic part θ_{p} is employed along with the moment M on the crack plane, computed from the load, to estimate the energy release rate J as

$J = J_e + J_p$, where,

$$J_e = \frac{K^2}{E}, \ J_p = \frac{\eta}{Bb} \int_0^{\theta_p} M d\theta_p, \tag{2}$$

are elastic and plastic contributions to J and the factor η is taken as 2 [40,41]. Trial and error calculations showed that neglecting J_e and computing J directly from the expression given above for J_p, by employing the total rotation θ, makes negligible difference especially at later stages because of profuse plasticity in the ligament.

2.2.2. Dynamic fracture tests

The dynamic fracture experiments are carried out using a Hopkinson pressure bar setup with aluminium bars of diameter 19 mm (see supplementary material). A single bar configuration without a transmitted bar is employed with the specimen supported against two cylindrical anvils which are fixed to a rigid frame. The load versus time history for the dynamic tests are obtained with the help of strain gauges fixed at the mid-length of the incident bar, which is 1.82 m long. A tup of diameter 6.35 mm is used at the end of this bar, and no plastic deformation is observed in it during the experiments. Also, no rotation constraint is imposed at the loading point. The striker bar is of length 45.7 cm. Dynamic tests are carried out at four loading rates by changing the striker bar velocity V_0 which, in turn, is achieved by adjusting the pressure in the gas gun. The values of V_0 corresponding to these four loading rates are about 9 m/s, 13 m/s, 17 m/s and 20 m/s, although there are slight variations amongst the multiple tests carried out for each case. The signals from the strain gauges are passed to an oscilloscope through an amplifier.

The incident and reflected pulses recorded by the strain gauges are used to obtain the applied load P as:

$$P = A_b E_b (\varepsilon_I + \varepsilon_R) \ . \tag{3}$$

Here, ε_I and ε_R are incident and reflected strain signals, respectively, which are suitably shifted to account for time lag caused by wave propagation in the incident bar and corrected for dispersion, A_b is the area of cross-section of the bar and E_b, its Young's modulus. The deformation of the specimen is recorded at the rate of 0.5 million frames per second with a resolution of 400 × 250 pixels using a Shimadzu HPV-X2 high speed camera (so as to capture the stress-wave dominant loading). In order to enable DIC analysis for obtaining displacements and strain fields, a speckle pattern is first applied on the specimen surface which is viewed by the high-speed camera. The energy release rate history, $J(t)$ is calculated using Eq. (2) as in the static analysis. To this end, the specimen rotation about the hinge point on the ligament, $\theta(t)$, is estimated from CMOD history $\delta_{\mathrm{m}}(t)$, which is extracted from the DIC analysis, along with Eq. (1). However, the contact load $P(t)$ obtained through Eq. (3) is not likely to be equilibrated with reactions imparted by the supports up to a certain time owing to inertial effects. The latter were measured by piezoelectric load cells mounted on the fixed supports which confirm that the end conditions are established during the course of the test.

The time over which inertial effects are expected to be dominant has been estimated by Nakamura et al. [39] and Ireland [42] as 2τ, where $\tau \sim 23\ W/c_o$, c_o being the elastic bar wave speed, is called as transition time [39] or inertial oscillation time period

Table 2
Test velocity, time to fracture, fracture mechanism, fracture toughness, average loading rate, critical CTOD, and twin area fraction near crack tip for static and dynamic tests.

Test Velocity, V_0 (m/s)	Time to fracture, t_f (μs)	Fracture Mechanism	Fracture Toughness, J_c (N/mm)	Average loading rate, j GN/ms	Critical CTOD, δ_{tc} (μm)	Twin area fraction near crack tip (%)
Static		Brittle	32±0.5		0.13	11.95±1.13
9	133±5	Ductile	60±1.5	0.45	0.24	7.58±0.3
13	103±7	Ductile	77±2.0	0.75	0.34	7.29±1.07
17	78±4	Ductile	81±1.5	1.03	0.39	5.00±0.4
20	65±1	Ductile	88±2.0	1.35		3.88±0.39

Note: Critical CTOD for $V_0 = 20$ m/s could not be reliably estimated due to loss in correlation in the images.

[42] of the specimen. For time $t < \tau$, the ratio of kinetic energy to strain energy of the specimen exceeds 1 and it decays to a value less than 0.2 only beyond a time of 2τ. As will be seen subsequently, the time corresponding to fracture initiation, t_f, for all dynamic tests conducted falls within the above noted time range of 2τ, which is estimated to be 160 μs for the present Mg alloy specimens. Hence, the measured contact load P is not directly used to compute the bending moment M about the hinge point on the crack plane but instead an alternate procedure proposed in [39] based on distribution of strains on a remote cross-section is employed. This is explained below, and more details are given in supplementary material.

Since the region around the ligament undergoes heavy plastic deformation, which makes precise evaluation of the strains near the crack tip and impact edge difficult, the bending moment and shear force, M and V over a cross-section located at a distance l (greater than $0.5b$) from the crack plane is first estimated. For this purpose, the strain variation on the specimen surface over such a cross-section, deduced from the DIC maps, is used along with a numerical algorithm to compute the normal (bending) and transverse (shear) stress distributions on the cross-section. This algorithm, which is based on polycrystal plasticity assuming Taylor homogenization, is given in the supplementary material. It makes use of single crystal plasticity constitutive equations at the level of individual grains, specific to Mg, which takes into account both dislocation slip on various systems and deformation twinning. The phenomenological hardening laws proposed by Zhang and Joshi [43] accounting for slip-slip, twin-twin and twin-slip interactions are incorporated in these constitutive equations. These rate equations are numerically integrated with respect to time using the rate tangent modulus algorithm of Peirce et al. [44]. The single crystal properties in the model are taken to be the same as those given in [17,45]. Also, a set of dominant lattice orientation extracted from the initial EBSD maps (Fig. 2(b)) are assigned to the grains that constitute the representative volume element (RVE) of the underlying microstructure in the homogenized polycrystal model (see [45] for the pole figures constructed from these extracted orientations).

The bending moment M about the hinge point on the crack plane is then obtained by the method explained in the supplementary material, which is based on a simple dynamic analysis of the beam-type specimen. In order to get a more robust estimate of M, a few cross-sections on either side of the crack plane with $l > 0.5b$ are considered and the average is taken. The above method is first applied to the static test data to evaluate M. This, along with the bending moment computed directly from the load for this test, are plotted (after smoothing) against the specimen rotation in Fig. 3(a). The two M - θ variations differ by less than 10%, which may be due to possible thickness dependence of strains and stresses that cannot be estimated from DIC analysis. The critical value of energy release rate, denoted as J_C, is ascertained as the value of J corresponding to the time at which the crack starts to grow in the static and dynamic tests. This stage is identified through careful visual inspection of the images captured during the test.

Each of the above experiments (static and dynamic) was conducted a few times in order to verify the repeatability of the results. In the static case and three of the dynamic tests ($V_0 = 9$ m/s, 17 m/s and 20 m/s), at least three experiments were performed, while for the case with $V_0 = 13$ m/s repeatability of the data was checked with two tests. The energy release rate histories ascertained from all the experiments conducted are presented in supplementary material and can be seen to be quite consistent with the J_c values for each loading case varying to within 5% (refer also Table 2).

2.3. Microscopic examination

Microstructural studies were carried out on the fractured specimens which were kept in a desiccator to prevent oxidation. Fractography was performed on a TESCAN VEGA 3 scanning electron microscope (SEM), with secondary electron imaging. Surface preparation for EBSD included mechanical polishing using silicon carbide abrasive paper and cloth polishing with diamond paste followed by electro-polishing. The electrolyte employed was composed of a 3:5 solution of orthophosphoric acid and ethanol. EBSD analysis was conducted on a TESCAN MIRA 3 SEM with a stage tilt of 70°, accelerating voltage of 25 kV, beam intensity 12 and a step size of 0.6 μm. Surface preparation for optical micrography included etching in addition to above mentioned polishing procedure. Etching was done using an acetic-picral etchant, for 5 s, to reveal the grain boundaries and twins. The optical micrography was carried out on LEICA DM 2700 M microscope at different magnification levels.

3. Results

3.1. Macroscopic response

Figs. 3(b) to (d) show M versus θ variations for dynamic experiments conducted at the three loading rates. It can be observed from these plots and the corresponding variation for the static case (Fig. 3(a)) that M increases steeply with θ initially and then tends to saturate at some level for $\theta > 0.04$ rad, owing to development of large scale yielding in the specimen (see Sec.3.2). On comparing the M-θ plots pertaining to the static and dynamic tests, it is evident that the saturation moment values are higher for the latter. Thus, the saturation value of M enhances from about 30 N-m for the static case (Fig. 3(a)) to around 45 N-m for the dynamic test with $V_0 = 20$ m/s (Fig. 3(d)). This enhancement is attributed to lattice reorientation in many grains caused by more pronounced tensile twinning near the loading-end of the ligament in the dynamic tests as will be seen in Sec.3.5. Thus, as the lattice in these grains reorients when TTs envelop them, hard systems like pyramidal $\langle c + a \rangle$ slip and CTs are activated which sharply increases the flow stress leading to a characteristic sigmoidal stress-

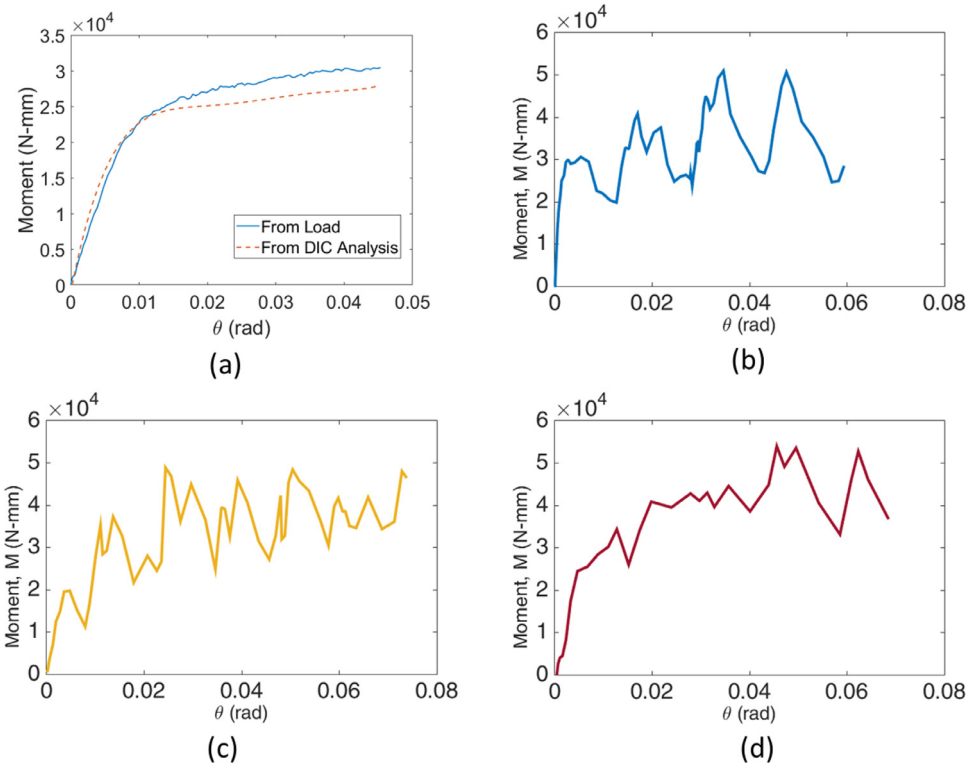

Fig. 3. Moment versus specimen rotation plots for (a) static test and the dynamic tests corresponding to (b) V_0 = 9 m/s, (c) V_0 = 13 m/s, and (d) V_0 = 20 m/s. The moment extracted from both DIC analyses as explained in Sec.2.2 and directly from load for the static case are shown in (a).

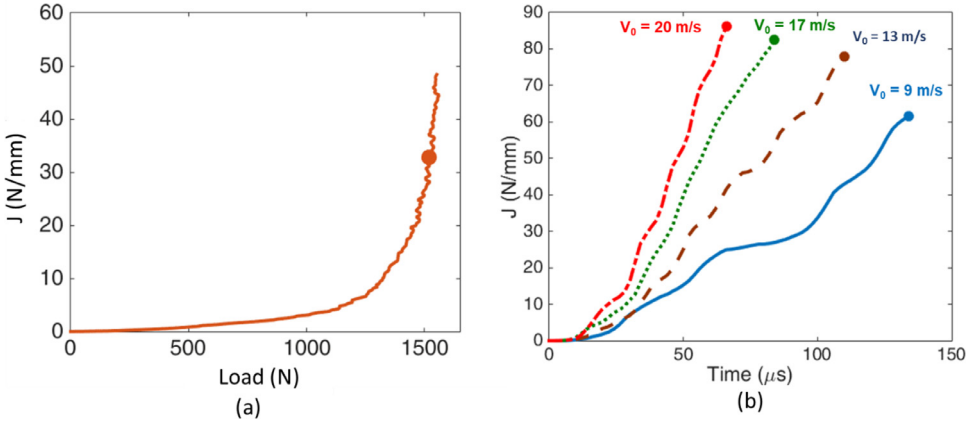

Fig. 4. Energy release rate histories for (a) static test as a function of load and (b) dynamic tests with different V_0 as functions of time.

strain curve under TD/RD compression (see, for example, [6,10]). Thus, it is expected that the magnitude of compressive normal stress on the ligament near the loading edge will be significantly higher in the dynamic tests at later stages, giving rise to much larger saturation bending moment as compared to the static tests.

Figs. 4(a) and (b) present the evolution histories of energy release rate (J) for the static and dynamic experiments, respectively. In these figures, J is plotted against load for the case of the static test and against time for the dynamic experiments. A filled circle (•) on all the curves shown in these figures indicates the crack initiation stage. It should first be noted from Fig. 4(a) that under static loading, J evolves slowly up to load of 1000 N and thereafter rises sharply owing to significant plastic deformation in the ligament. Fig. 4(b) indicates that J increases appreciably faster with respect to time as the impact speed V_0 increases.

For example, corresponding to t = 50 μs, the value of J enhances from 15 to 53 N/mm as V_0 changes from 9 to 20 m/s. On further examining Fig. 4(b), it can be noted that fracture toughness J_c (refer to the stages marked by '•' symbols) increases strongly with V_0, while the time to fracture, t_f, reduces. The values of J_c and t_f pertaining to all tests conducted are presented in Table 2 along with the average loading rate, $\dot{J} = J_c/t_f$. It can be noted from this table that as V_0 changes from 9 to 20 m/s, J_c enhances from 60 to 88 N/mm, whereas t_f reduces from 133 to 65 μs. Thus, the highest average loading rate generated in these dynamic fracture tests is $\dot{J}$ = 1.35 GN/ms. By contrast, the static fracture toughness is only 32 N/mm, which is about half of that pertaining to V_0 = 9 m/s case. A qualitatively similar trend in variation of K_c with loading rate was reported by Yu et al. [37] from their dynamic experiments conducted on AZ31B Mg alloy using three-point bend specimens with crack line along ND and span along RD.

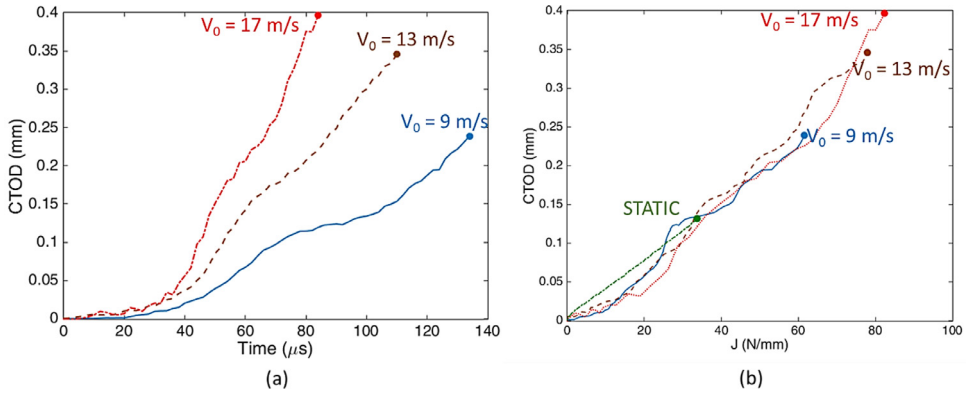

Fig. 5. CTOD measured at a distance of 150 μm behind the crack tip for different tests plotted as functions of (a) time and (b) energy release rate. (For interpretation of the references to colour in this figure legend, the reader is referred to the web version of this article.)

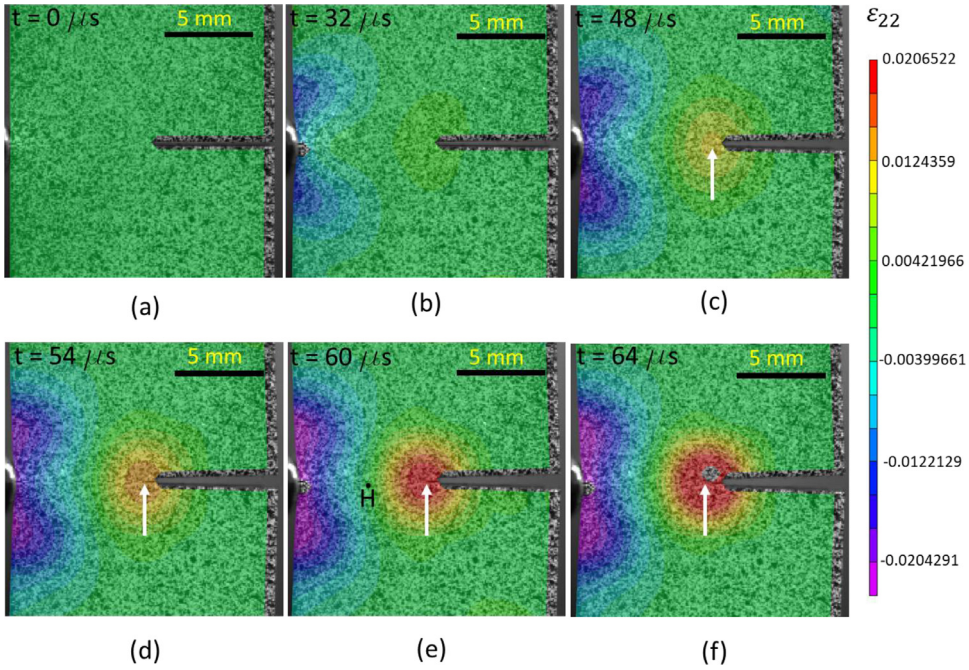

Fig. 6. Normal strain (ε_{22}) contours at different time instants for a dynamic test with V_0 = 20 m/s corresponding to (a) t = 0 μs, (b) t = 32 μs, (c) t = 48 μs, (d) t = 54 μs, (e) t = 60 μs and (f) t = 64 μs. The crack tip location is indicated by vertical white arrow in (c)-(f), and the hinge point as H in (e). (For interpretation of the references to colour in this figure legend, the reader is referred to the web version of this article.)

The evolution of crack tip opening displacement (CTOD), δ_t, measured at 150 μm behind the pre-crack tip, with time is presented in Fig. 5(a). As in the case of Fig. 4, a filled circle (•) on all the curves shown in this figure indicates the crack initiation stage. It can be observed that rate of increase of CTOD with time as well as the CTOD at crack initiation increase with loading rate. For example, at t = 50 μs, δ_t enhances from 0.04 to 0.15 μm, while the critical CTOD at crack initiation, δ_{tc}, increases from 0.24 to 0.39 μm as V_0 changes from 9 to 17 m/s (see also Table 2, where the latter values are summarized). It is important to note by comparing Figs. 5(a) and 4(b) that time histories of CTOD and J pertaining to different V_0 are qualitatively similar. Hence in Fig. 5(b), CTOD is plotted against J, corresponding to the static and dynamic tests, in order to examine the correlation between these two important fracture characterizing parameters [35,46–48]. Indeed, the plots displayed in Fig. 5(b) do show a reasonable linear dependence of δ_t (measured directly using DIC) and J (determined by applying Eq. (2)) for all tests. This corroborates with the work of Shih [47] based on HRR solution [35,48] and therefore lends confidence to the methodology adopted in this work to estimate the latter.

3.2. Normal strain distribution on specimen surface

Fig. 6(a) to (f) show contours of normal strain ε_{22}, deduced from DIC analysis, on the specimen surface, corresponding to a sequence of time instants from beginning of loading up to crack initiation stage for a typical dynamic test conducted with striker velocity V_0 = 20 m/s. These strain contours confirm that the DIC analysis of the images acquired using the high speed camera can indeed delineate the stress wave dominant loading experienced by the specimen since the time range over which these plots are shown falls within τ. On examining Fig. 6(b), it is evident that a compressive strain field begins to develop near the loading-edge of the ligament following impact by the incident bar. At t = 48 μs, Fig. 6(c) shows two distinct symmetric lobes of strain have formed at the

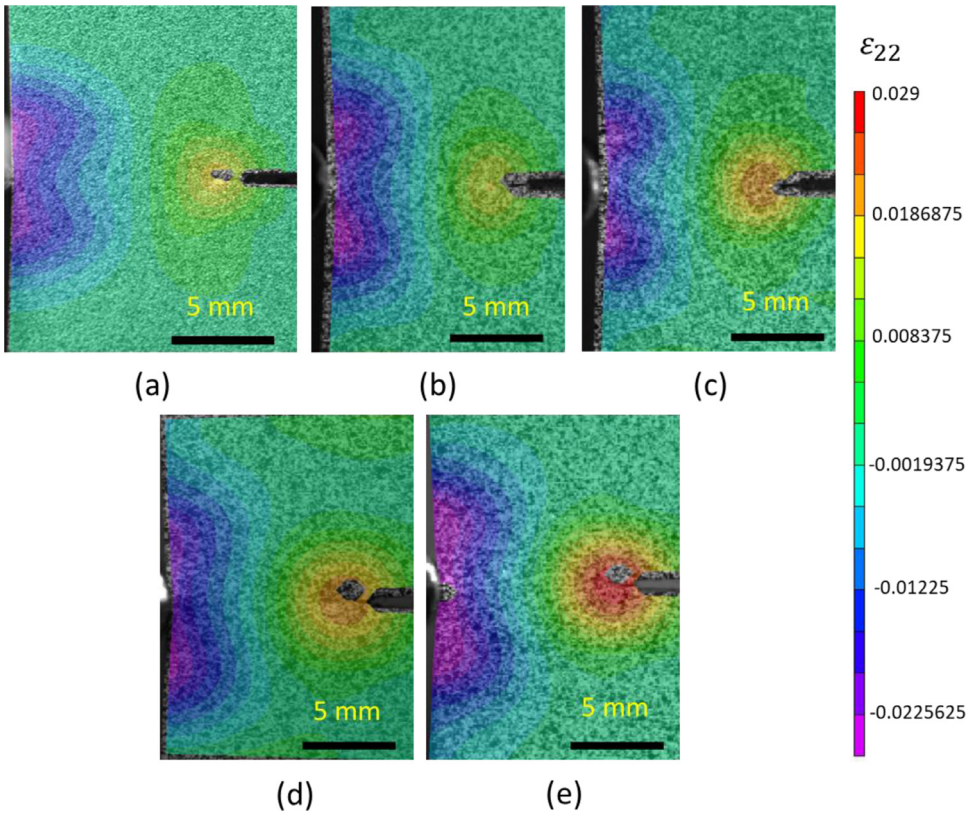

Fig. 7. Normal strain (ε_{22}) contours at crack initiation stage for: (a) static test, and dynamic tests with (b) V_0 = 9 m/s, (c) V_0 = 13 m/s, (d) V_0 = 17 m/s, (e) V_0 = 20 m/s. (For interpretation of the references to colour in this figure legend, the reader is referred to the web version of this article.)

far-edge, whereas a perceptible tensile strain field also starts to envelop the crack tip (indicated by white vertical arrow). With further increase in time, the compressive strain field at the far-edge of the ligament and the tensile strain field near the crack tip enhance in magnitude and spread over larger regions (Fig. 6(d), (e)). Also, the two strain lobes at the far-edge merge together to form a roughly semi-circular shape (Fig. 6(e)). Thus, Fig. 6(e) shows a well developed bending strain field in the ligament with the hinge point (where reversal in sign of normal strain on the ligament occurs) located at H (which is about 0.4b from the crack tip). The strain contours near the crack tip are rounded in shape, which is typical of the plane stress condition that is expected on the specimen surface [49]. Fig. 6(f) depicts the stage just after crack initiation, with a significantly intensified strain field near the crack tip and some loss of correlation that has occurred in the DIC strain map owing to crack extension from the initial crack tip (see vertical arrow).

The normal strain (ε_{22}) contours at the crack initiation stage for all the tests are presented in Figs. 7(a) to (e). These images indicate that the strain distribution on the specimen surface is qualitatively similar for the static and all dynamic tests. However, it is important to note that the magnitude of tensile strain prevailing near the crack tip at the initiation stage enhances strongly with loading rate (compare Fig. 7(e) with 7(a) and (b)). This implies strain (and stress) intensification close to crack tip at high loading rates (specifically, for V_0 = 17 and 20 m/s). Concurrently, examination of the loading-edge of the ligament shows that the magnitude of compressive strain in this region also enhances appreciably at high V_0 (see Fig. 7(e)) and the size scale over which it prevails is also larger. This has an important bearing on the dissipation due to plastic work occurring in the far-field region with increase in loading rate, which as will be seen below, is caused by profuse tensile twinning.

3.3. Fractography

The fractured surfaces of the broken specimens are examined using a SEM to gain insights on the operative fracture mechanism. Figs. 8(a)-(c) display fractographs taken with 1000x magnification close to the fatigue pre-crack front near the mid-plane of the specimens corresponding to the static and dynamic tests with V_0 = 9 m/s and 17 m/s. The fatigue pre-crack front is near the bottom edge of these images (see white dashed lines) and the crack propagates upward as indicated by the black arrow at the extreme left of the figure. A distinct difference in the fracture surface morphology near the initial crack front can be perceived between the static and dynamic tests. Thus, the fracture surface pertaining to the former (Fig. 8(a)) is decorated predominantly with quasi-brittle features like elongated grooves or flutes such as those labeled as A, B and C, which are believed to be induced by tensile twins [3,12,13,15]. These features, which are quite different from the shallow striation-like impressions seen in the fatigue pre-crack region (below the white dashed line in Fig. 8(a)), were labeled as Cleavage 3 regime in the fracture mechanism maps pertaining to Mg alloys by Gandhi and Ashby [50]. Kaushik et al. [13] conducted experiments using notched three-point bend specimens of Mg single crystal and noted that the crack grows along twin boundaries with deflections at twin-twin intersections. They reported elongated stripes or grooves on the fracture surface and concluded that these form by intersection of twins (of another variant) on the fracture surface. Similar groove-like features on the fracture surface were also noted in [12,15] from static fracture tests using fatigue pre-cracked specimens and by Kondori and Benzerga [3] from cylindrical tensile specimens with fine circumferential notches of AZ31 Mg alloy. By contrast, far few dimples were observed on the fracture surfaces of the statically loaded specimen.

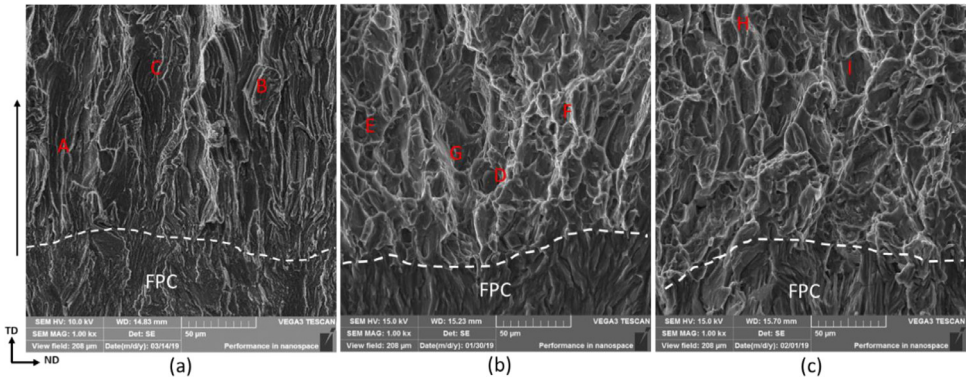

Fig. 8. SEM fractographs near fatigue pre-crack (FPC) front (white dashed lines) taken with 1000x magnification corresponding to: (a) static test and dynamic tests with (b) $V_0 = 9$ m/s, (c) $V_0 = 17$ m/s. Crack propagation direction is vertical as indicated by the arrow on the left.

On the other hand, the fracture surfaces pertaining to the dynamically loaded specimens (Figs. 8(b) and (c)) display no such twin-induced brittle features but instead show a distribution of micro-voids. In order to quantify the difference between the fracture morphology seen in these figures and the static case (Fig. 8(a)), surface roughness (R_q) measurements were made over square regions of size 500 μm using an optical profilometer with a resolution of 50 nm. However, the R_q values were found to be about the same (~ 8.5 μm) for the static and dynamic test with $V_0 = 9$ m/s, whereas it was markedly lower (~3.8 μm) for a test corresponding to $V_0 = 13$ m/s, which only indicates that the dimples are shallow for the higher impact speed case. As an alternative distinguishing measure of the fractographic features, their aspect ratio was quantified by identifying 100 such features for each loading case and tracing them with Image-J software (see supplementary material). The average aspect ratios were found to be 6, 1.6 and 1.3 for the specimen tested under static loading and dynamic loading with $V_0 = 9$ and 17 m/s, respectively. These values confirm that the fractographic features are highly elongated grooves/flutes for the static case, whereas they are more rounded in the dynamically loaded specimen, which along with the visual examination of Figs. 8(b) and (c), attests that they are dimples.

Further confirmation that (the almost) equi-axed features such as those labeled as D, E, F (Fig. 8(b)), I and H (Fig. 8(c)) are voids stems from the fact they seem to have been nucleated by fracture / debonding of inclusions (see, for example, E in Fig. 8(b)). EDS analysis conducted here and in previous studies [3,20] show that these void nucleating particles in AZ31 Mg alloys are pure Mn or Al-Mn (about 25% Al, 70% Mn and 5% Mg by weight), $Mg_{17}Al_{12}$ intermetallics and oxides (MgO). Most of these voids have coalesced with neighboring ones by complete internal ligament necking, resulting in knife-edge like features at their periphery (such as E, H and I). A few tear-ridges characteristic of abrupt rupture of inter-void ligaments are occasionally noticed (like G in Fig. 8(b)). Although there is a large scatter in the void sizes for each loading case, their average diameter is found to increase from 6 to 9 μm as V_0 changes from 9 m/s to 20 m/s.

Figs. 9(a), (b) and (c) show fractographs (1000x magnification) taken at a distance of 1.5 mm ahead of the fatigue pre-crack front near the specimen mid-plane corresponding to static and dynamic tests with $V_0 = 9$ m/s and 17 m/s. It can be observed by comparing Fig. 8(a) and 9(a) that the fracture surface features pertaining to the static test have changed with crack growth. Thus, unlike Fig. 8(a), many micro-voids (such as those indicated as K, L and M) can be noticed in Fig. 9(a) with evidence of fractured particles in some cases (see M) along with a few brittle features like that indicated as J. The latter are far more numerous close to the initial crack front (Fig. 8(a)). Thus, a brittle to ductile transition seems to have occurred with crack extension in the static experiment, which was also reported by Prasad et al. [15] in their static fracture tests with fatigue pre-cracked four-point specimens. On the other hand, the fractographs pertaining to the dynamic tests continue to show dimples far ahead of the initial crack front as well (Fig. 9(b), (c)). In fact, some large voids with fractured particles inside them (like N and O) can be noticed in Fig. 9(b). As in the case of the region near the pre-crack front (Fig. 8(b), (c)), only a few tear ridges (such as P in Fig. 9(b)) can be seen and most voids have coalesced by complete internal ligament necking.

3.4. Optical micrographs of deformed specimens

In Figs. 10(a) and (b), low magnification optical images of a deformed specimen corresponding to a static test and the two halves of a fractured specimen obtained after a dynamic test conducted with $V_o = 17$ m/s are shown. Specimens are polished and etched following the procedure outlined in Section 2.3, in order to reveal the nature of inelastic deformation.

A large, roughly semi-circular bright region can be noticed in both specimens spreading downwards from the (upper) loading edge (Figs. 10(a) and (b)). Further, a curious pattern of curved bands resembling fingers can be observed near the bottom portion of the above bright region. The static specimen (Fig. 10(a)) also shows a bright deformed region enveloping the crack tip near the lower edge. In order to understand how the above noted bands form near the loading edge, one of the static tests was interrupted and the specimen was unloaded. It was then optically imaged after following the usual polishing / etching protocol. This deformed specimen, which is displayed in Fig. 10(c), reveals a set of parallel white bands that are roughly equally spaced extending downwards from the top edge. With continuation of loading, these bands apparently widen and merge with each other, except near the bottom portion where they retain their discrete shape, forming the bright semi-circular zone observed in Figs. 10(a) and (b).

A small region encompassing the bands in the bottom portion of the bright semi-circular region, within the blue rectangular box indicated in Fig. 10(b), is examined under a high resolution optical microscope. This optical micrograph is presented in Fig. 10(d) and shows two parallel bands, whose boundaries are marked by red dashed lines, which are several grain sizes in width containing a high density of tensile twins. The region between these bands, which has both small and big grains and is also several grain sizes in width, is completely free of twins. A careful examination of the two twin bands in Fig. 10(d) reveals that the twins extend roughly parallel to the orientation of the band and as continuous chains spreading across grain boundaries. Possible reasons for the origin

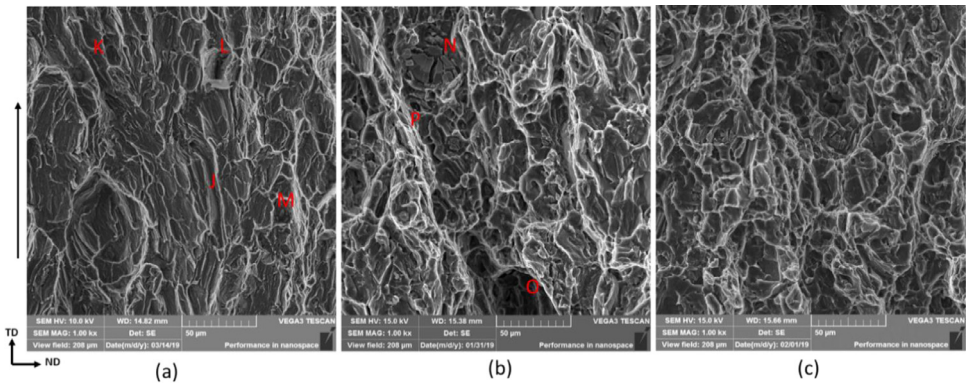

Fig. 9. SEM fractographs about 1.5 mm away from original crack front taken with 1000x magnification corresponding to: (a) static test and dynamic tests with (b) $V_0 = 9$ m/s, (c) $V_0 = 17$ m/s. Crack propagation direction is vertical as indicated by the arrow on the left.

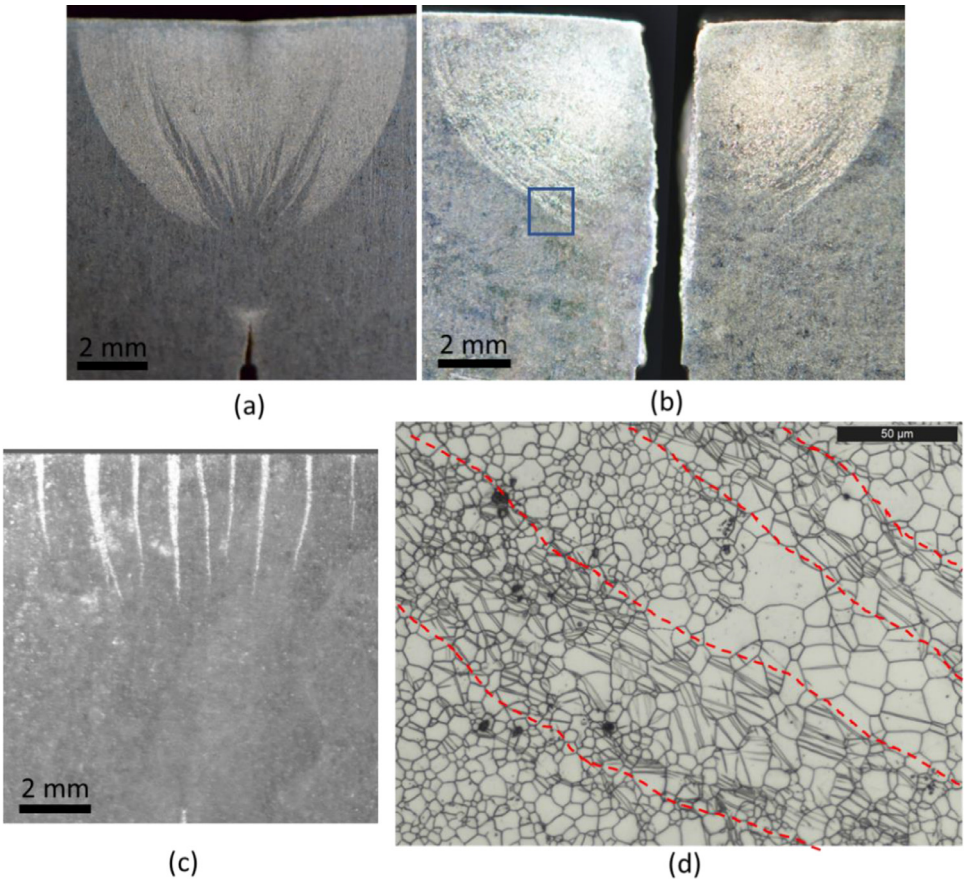

Fig. 10. Optical images showing deformed specimen corresponding to (a) static test, (b) dynamic test with $V_0 = 17$ m/s (both fractured halves) and (c) a static test after interrupting and unloading. (d) A higher magnification optical micrograph corresponding to a small region within the blue rectangular box marked in (b) showing two twin bands. (For interpretation of the references to colour in this figure legend, the reader is referred to the web version of this article.)

of these tensile twin bands and their influence on the fracture resistance of the Mg alloy will be discussed in Sec. 4.

In Fig. 11(a), an optical micrograph taken near the crack tip after a short extension is shown. In this micrograph, the crack line can be seen at the bottom left corner, with the current crack tip indicated by a red horizontal line. Considerable twinning can be perceived in grains surrounding the tip spreading up to a distance of about 100 µm ahead of the tip and 150 µm in the direction normal to the crack line. Analysis of EBSD maps (see Sec.3.5) confirms that these are tensile twins. In fact, some grains have multiple intersecting twins (see grain marked as Q) and several parallel twins, possibly of the same variant (grain identified as R). Also, some of the twins extend across grain boundaries (see location indicated as S) similar to Fig. 10(d). In Fig. 11(b), an optical micrograph of the region near the initial crack tip, obtained from one of the broken halves of a specimen tested under dynamic loading with $V_0 = 17$ m/s, is displayed. Here, the crack line is along the right vertical boundary of the image and the approximate location of the initial crack tip is marked by a red horizontal arrow. In contrast to Fig. 11(a), very few twins may be noticed in the grains above and to the side of the initial crack tip. This suggests that there is a reduction in amount of twinning around the original tip with enhancement in loading rate. In order to confirm this, rectangular domains of size 200 µm × 170 µm close to the initial crack

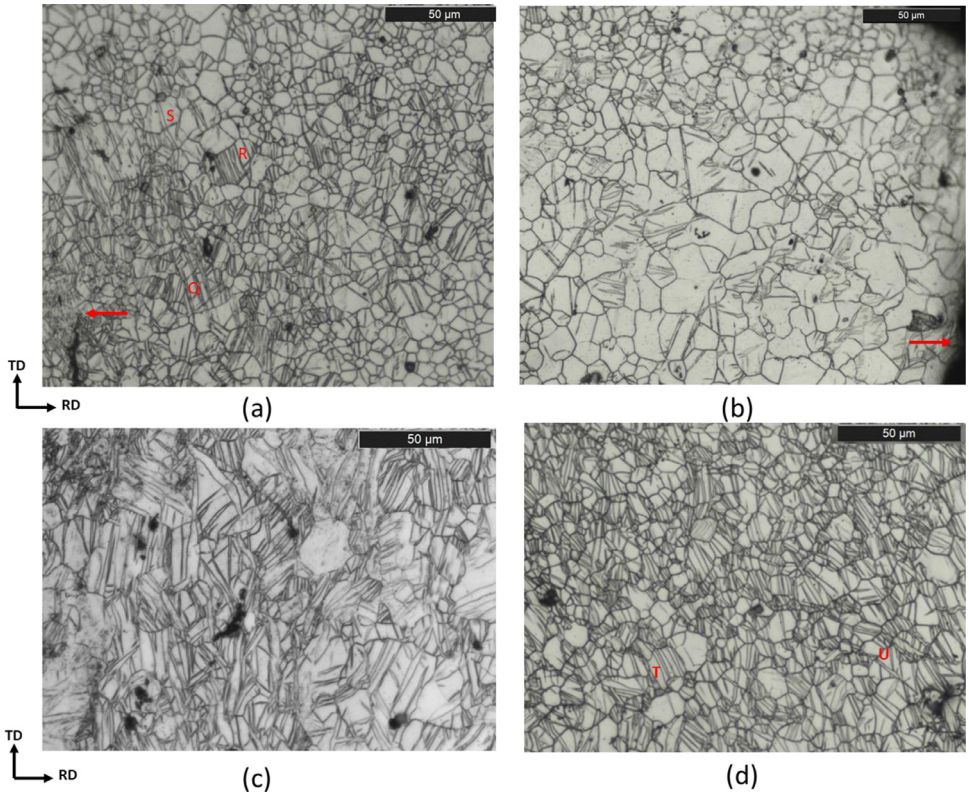

Fig. 11. Optical micrographs near crack tip corresponding to (a) static test and (b) dynamic test with V_0 = 17 m/s. Optical micrographs near the far-end of the ligament close to loading edge corresponding to (c) static test and (d) dynamic test with V_0 = 17 m/s.

tip (like the optical images shown in Fig. 11(a), (b)) were analyzed using the point count method (ASTM E562–19 [51]) and the average twin area fraction was estimated. These values are given in Table 2, and can be observed to decrease from about 12% for static loading to 4% for the dynamic test with V_0 = 20 m/s.

Figs. 11(c) and (d) show optical micrographs obtained from the loading-end of the ligament (refer to the top edge of bright region in Figs. 10(a), (b)), corresponding to the static and dynamic test with V_0 = 17 m/s, respectively. Both these micrographs indicate massive twinning at the far-end of the ligament with many grains having multiple parallel twins (see, for instance, grain T in Fig. 11(d)) and intersecting twins (grain U in Fig. 11(d)). Twins extending across boundaries of multiple grains (see the ones adjacent to grain T in Fig. 11(d)) can also be perceived. Again, EBSD maps confirm that these are tensile twins, and as will be seen below, result in strong changes in the texture in this region.

3.5. EBSD maps near crack tip and specimen far edge

In Fig. 12(a), the IPF map near the extended crack tip along with (0001) and $(11\bar{2}0)$ PFs corresponding to a static test are shown. The crack that has extended in the vertical direction can be seen in the IPF image. Similar IPF maps and PFs pertaining to the region near the initial crack tip, extracted from one of the broken halves of specimens subjected to dynamic loading with V_0 = 9 and 17 m/s are presented in Fig. 12(b) and (c), respectively. In these IPF maps, the initial crack is along the lower edge of the image. The IPF map corresponding to the static test (Fig. 12(a)) shows that most grains continue to remain in the initial (almost basal) orientation. However, the grains present on the sides of the crack line and up to a distance of about 100 μm ahead of it are populated with deformation twins. Analysis of the angle change of the lattice within these twins, with respect to the parent grain indicates that it is about 86°, which confirms that these are TTs. By contrast, fewer twins are noticed in the grains near the initial crack tip from the IPFs pertaining to the dynamic tests (see Figs. 12(b) and (c)). In fact, hardly any twins are visible in the IPF corresponding to V_0 = 17 m/s (Fig. 12(c)). This corroborates with the reduction in average twin area fraction estimated from the optical micrographs taken near the crack tip. On comparing the PFs displayed in Fig. 12 with those pertaining to the undeformed specimen (Fig. 2), it can be noticed that for the statically tested specimen and dynamic case with V_0 = 9 m/s, some of the basal poles have tilted from near ND towards RD (see, in particular, (0001) PFs shown in Figs.12(a), (b)). However, the overall texture changes are small for the specimen tested with V_0 = 17 m/s (Fig. 12(c)).

The IPF maps and PFs obtained from the region adjacent to the loading-end of the ligament for a static test and dynamic tests performed with V_0 = 9 and 17 m/s are displayed in Figs. 13(a)-(c), respectively. It can be noted from Fig. 13(a) that most of the grains, which were initially in near- basal orientation, have multiple parallel or intersecting twins as noted from the optical metallograph presented in Fig. 11(c). As compared to the (0001) PF taken from the region close to the crack tip (Fig. 12(a)), many basal poles have shifted to the periphery in the PF shown in Fig. 13(a), although a strong concentration of these poles at the center (i.e., close to ND) is still present. Perceptible change in the $(11\bar{2}0)$ PF in comparison to the initial one (Fig. 2) can also be noticed from Fig. 13(a). On examining the IPF for the case V_0 = 9 m/s (Fig. 13(b)), it can be seen that the population of TTs is higher compared to the static case. In fact, the lattice in some grains, such as those marked by V and W, have almost completely re-oriented due to tensile twinning (although a small portion of the latter grain still appears to be in the initial near-basal orientation). The PFs pertaining to this case show more profound changes from the initial ones as compared to the statically tested specimen (Fig. 13(a)). Thus, the (0001) PF in

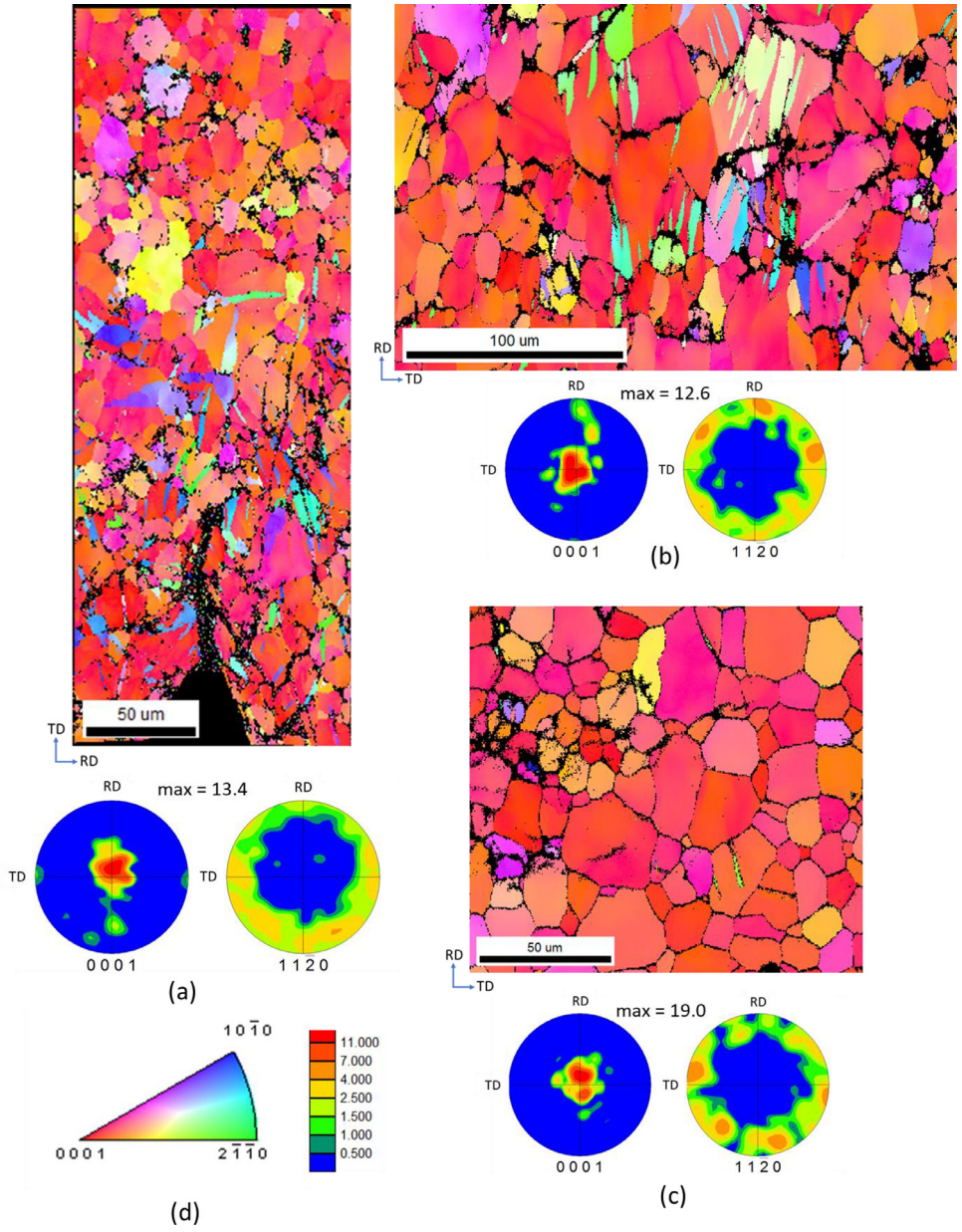

Fig. 12. IPF maps and PFs extracted near the initial crack tip corresponding to (a) static test and dynamic test with (b) V_0 = 9 m/s, (c) V_0 = 17 m/s. (d) Legends for IPFs and PFs. (For interpretation of the references to colour in this figure legend, the reader is referred to the web version of this article.)

Fig. 13(b) indicates that the intensity of poles at the periphery is more appreciable compared to Fig. 13(a) and that at the center has decreased. The (11$\bar{2}$0) PF also exhibits stronger changes (compare with Fig. 2).

Finally, turning to Fig. 13(c) pertaining to the specimen tested with V_0 = 17 m/s, it can be observed from the IPF that in almost all grains, the lattice has completely re-oriented so that ND is along [11$\bar{2}$0] or [10$\bar{1}$0] direction, due to tensile twins fully enveloping these grains. The (0001) PF confirms this observation with concentration of poles seen at the periphery, whereas there is negligible intensity at the center. The (11$\bar{2}$0) PF also indicates a strong intensity at the center in contrast to the initial one (refer Fig. 2) where this was negligible. *Thus, Fig. 13 shows that the density of tensile twins and the associated changes in texture near the loading edge for the dynamically tested specimens are more profound than the static ones and, in fact, enhance with impact velocity.* This is consistent with the higher (compressive) normal strain levels observed in the above region at crack initiation as the loading rate increases (refer Fig. 7).

4. Discussion

4.1. Effect of loading rate on fracture mechanism

As noted in Sec.3.3, the SEM fractograph near the fatigue pre-crack front corresponding to the static test (Fig. 8(a)) shows predominantly quasi-brittle features like elongated grooves or slits which have been traced to twin-induced brittle cracks [3,12,13,15,50]. Indeed, the optical micrographs and IPF maps for the static tests exhibit a fairly high average area fraction of TTs in the neighborhood of the crack tip (Figs. 11(a) and 12(a)), which reinforces the inference based on the fractographs. On the other hand, in the dynamic tests, the TT area fraction around the crack tip diminishes (see Table 2). Concurrently, the fractographs (Fig.

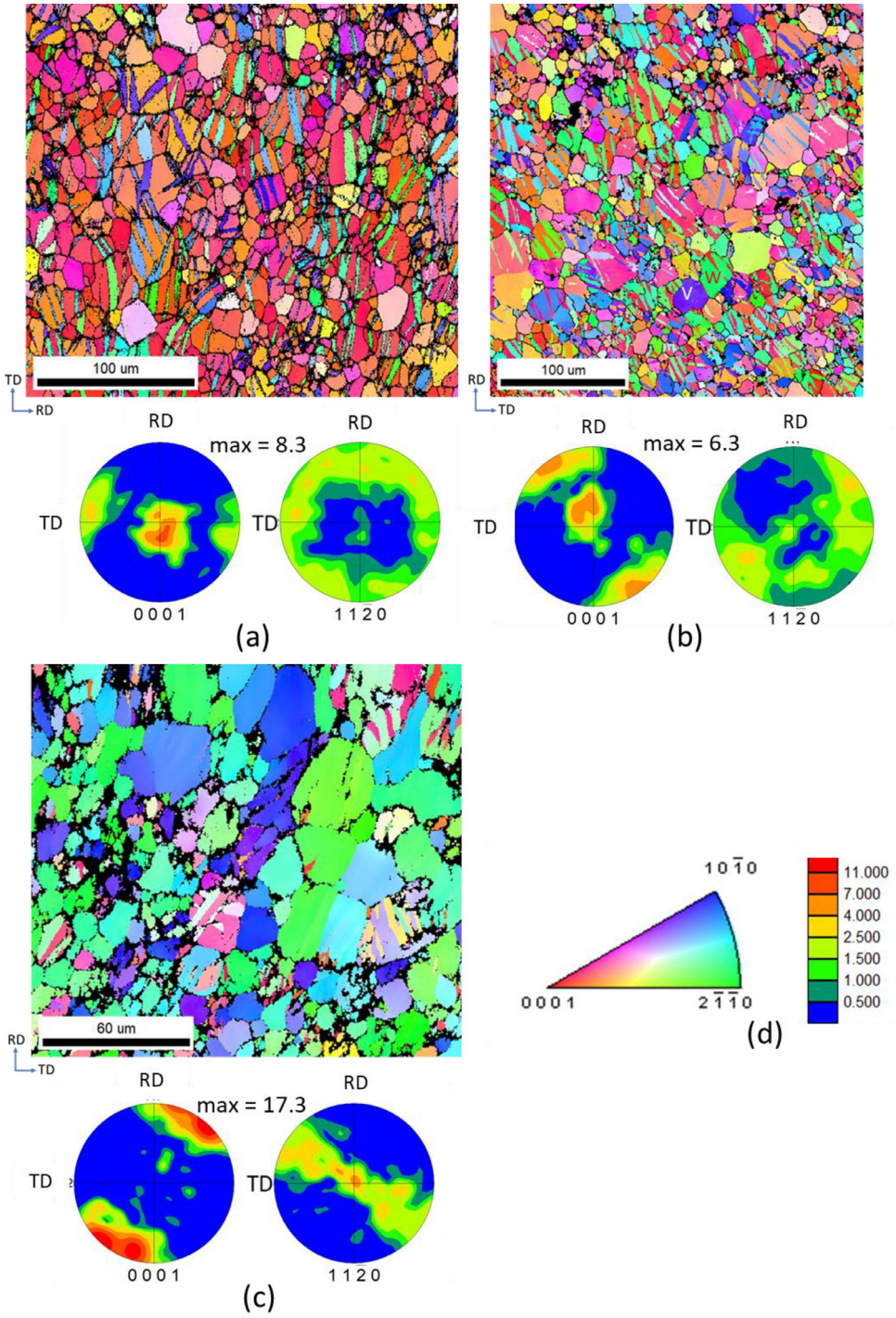

Fig. 13. IPF maps and PFs near loading edge corresponding to (a) static test and dynamic tests conducted with (b) $V_0 = 9$ m/s, (c) $V_0 = 17$ m/s. (d) Legends for IPFs and PFs. (For interpretation of the references to colour in this figure legend, the reader is referred to the web version of this article.)

8(b)-(c)) display nearly equi-axed dimples, which establishes that a quasi-brittle to ductile transition in fracture mechanisms occurs as loading changes from static to dynamic in the present experiments.

In order to rationalize these trends, it is important to first recall that previous static tests [3,15] have shown similar fracture mechanism transition as notch acuity (or near-tip stress triaxiality) is reduced from high to moderate levels. Further, it was noted in [15] that the average twin area fraction in grains around the tip drops from 13.5% for a fatigue pre-cracked bend specimen to 6.8% for a notched specimen with root radius of 60 μm. CPFE computations [17] of the experiments reported in [3] have also indicated similar reduction in TT volume fraction between a sharply notched cylindrical RN-2 specimen and moderately notched RN-10 specimen (which display above noted fracture mechanism transition). At a more fundamental level, it has been postulated that TTs are triggered by pile-up of basal dislocations at grain boundaries [45,52]. Thus, it may be concluded that as stress triaxiality near a notch or crack tip decreases from high to moderate levels: (a) twin density near the tip diminishes and (b) quasi-brittle to ductile fracture mechanism transition occurs in this Mg alloy.

As mentioned earlier, the ratio of $t/(2\tau)$, governs the effect of material inertia on the macroscopic specimen response, while $\dot{K}_I$ or $\dot{J}$ controls local inertial influence on near-tip fields. Also, the computational studies reported in [29–33] have shown that for $t < 2\tau$, the fracture specimen loses constraint which manifests in terms of negative *T*-stress or triaxiality parameter *Q*. Moreover, the magnitude of this constraint loss during the above time window enhances with $\dot{K}_I$ or $\dot{J}$. This is somewhat similar to the effect of local material inertia on necking in notched elastic-plastic bars, wherein one of the important parameters is the ratio of imposed velocity to elastic wave speed [53].

Further, in all the dynamic fracture experiments conducted in the present study $t_f/(2\tau) < 1$, and $\dot{J}$ is of the order of 0.5 GN/(ms) or higher (see Table 2). From the elastic-plastic finite element analysis reported in [30] for a three point bend specimen with $a/W = 0.5$, the drop in near-tip hydrostatic stress, with respect to static case, is found to be around $0.6\sigma_0$ corresponding to dynamic loading with $\dot{J}$ of 0.5 GN/(ms), where σ_0 is the tensile yield strength. This confirms that stress triaxiality will be lowered by an amount similar to that between the RN-2 and RN-10 notched cylindrical specimens tested in [3] which triggered fracture mechanism transition in this alloy. This explains the origin of the above transition seen between the static and dynamically loaded specimens (even with $V_0 = 9$ m/s) mentioned above. These features are illustrated schematically in Fig. 14(a) and (b). For the statically loaded specimen, *high stress triaxiality caused by the J-dominant HRR field [48] prevailing outside the fracture process zone (FPZ) close to the crack tip may be responsible for activating the TTs* and consequent quasi-brittle failure (Fig. 14(a)). On the other hand, *the two-parameter J-Q field [34,35] exists near the tip in the dynamically loaded specimens, with the triaxiality parameter Q becoming increasingly negative as* $\dot{J}$ *enhances [29–33]*, effecting the change to slow void growth and coalescence in the FPZ (Fig. 14(b)).

4.2. Dependence of fracture toughness on loading rate

A strong enhancement in fracture toughness J_c, with loading rate is observed for the present Mg alloy. Thus, there is an almost 200% increase in J_c corresponding to the dynamic tests with $V_0 = 20$ m/s as compared to static loading. This enhancement is higher than in many other engineering alloys [24–28]. The pronounced increase in J_c with $\dot{J}$ for the present AZ31 Mg alloy can be rationalized by noting that the contribution to fracture toughness arises from two sources, viz., intrinsic work of separation in the fracture process zone, denoted here as J_c^{fp}, and from background plastic dissipation, indicated as J_c^{bp}. As will be discussed below, the evidence presented in Sec.3 demonstrates that both these components increase with loading rate.

4.2.1. Contribution to toughness from intrinsic work of separation J_c^{fp}

The contribution from intrinsic work of separation depends on the operative fracture mechanism. As noted in Sec.4.1, this mechanism changes from quasi-brittle to ductile as loading changes from static to dynamic. Moreover, in the context of isotropic plastic solids, it has been noted that ductile fracture processes will be impeded as loading rate enhances owing to higher levels of negative *Q* caused by inertial effects [30,36]. This corroborates with retardation in void growth as triaxiality drops which has been observed for both isotropic plastic solids [54] and Mg single crystals [21,22]. An added factor is strain rate sensitivity which was shown in [36] to further slow down void growth under dynamic loading.

The above noted drop in near-tip stress triaxiality would translate in terms of elevation in J_c^{fp} as shown by Prasad et al. [15] from their static fracture tests with increase in notch root radius. An approximate estimate of this enhancement can be made by considering for example the case $V_0 = 9$ m/s, for which the average $\dot{J} \sim 0.45$ GN/(ms). As mentioned above, elastic-plastic finite element computations [30] have shown that $Q \sim -0.6$ for a similar specimen corresponding to this level of $\dot{J}$. Further, for a rolled AZ31 Mg alloy, Prasad et al. [15] reported an enhancement in J_c^{fp} under static loading by about 25 N/mm as notch root radius increases from 30 μm to 100μm (see Fig. 4 of their paper). The reduction in hydrostatic stress associated with the above change in notch root radius in the vicinity of nearest void nucleating inclusion ahead of the notch tip in their alloy (spacing about 35μm [15]), can be evaluated following the slip-line field of Rice and Johnson [55], as about $0.6\sigma_0$. Thus, the above approximate calculation shows that even for the case $V_0 = 9$ m/s, a strong enhancement in J_c^{fp} of about 25 N/mm may be expected owing drop in near-tip stress triaxiality.

The above features anticipated in the variation of J_c^{fp} with *Q* are schematically illustrated in Fig. 15. Also indicated in this figure are the specific values of J_c^{fp} pertaining to the static case (where $Q = Q_s$) and under dynamic loading with increasing $\dot{J}$ (where *Q* becomes progressively more negative so that $Q_3 < Q_2 < Q_1$). As is clear from this schematic, J_c^{fp}will enhance with $\dot{J}$ and the brittle-ductile transition would further accentuate the contribution to the dynamic fracture toughness from the near-tip fracture processes as compared to J_{cs}^{fp}.

4.2.2. Contribution to toughness from background plastic dissipation

A major contribution to fracture toughness, J_c^{bp}, arises from dissipation in the background plastic zone, which includes the inelastic deformation processes of slip and twinning. The DIC strain maps presented in Fig. 6 and 7 indicate that strong plastic deformation occurs in the region around the crack tip as well as close to the loading edge. The optical images, Fig. 10(a), (b) show a large bright semi-circular zone near the loading-edge of the ligament, which under high resolution microscopy reveals tensile twins forming in bands (Fig. 10(d)). This intriguing pattern of twin bands was also observed by Baird et al. [56] in thin, unnotched AZ31 Mg alloy sheet specimens under three-point bending. Under this loading condition, the far-field region is subjected to compression normal to the ligament (note from Fig. 7 that ε_{22} is negative in this region). Due to the near-basal texture of this alloy, with c-axis aligned close to ND, the above compression normal to the ligament favours formation of TTs in this region to accommodate the expected out-of-plane bulging of the specimen. Here, it is to be noted that, in addition to variation in lattice orientation and therefore the Schmid factor for TTs, the critical resolved shear stress (CRSS) associated with twinning is also expected to vary due to the variation in grain size (bimodal grain size distribution of the present alloy) with the larger grains having lower CRSS values [57]. Thus, the average initial spacing between the twin bands seen in Fig. 10(c) would be determined by the spatial fluctuation in ratio of Schmid factor to CRSS for tensile twinning.

The TTs thus nucleated adjacent to the loading edge, extend across the grains before getting arrested at their boundaries. The stress concentration created at the arrested twin tips nucleate twins in the adjacent grains and the process repeats forming continuous bands of twins spreading across several grains as seen in Fig. 10(c) and (d). These bands widen and merge with further loading enveloping the entire region in the upper part of the specimen (above the plastic hinge point). This far-field plastic region, characterized by profuse twinning, is indicated in the schematics displayed in Fig. 14(a) and (b).

Fig. 7 shows that at crack initiation, the intensity of normal strain both in the crack tip plastic zone and far-field region, as well as the extent over which they prevail enhance with loading rate. Moreover, the IPF maps (Fig. 13) indicate progressively higher

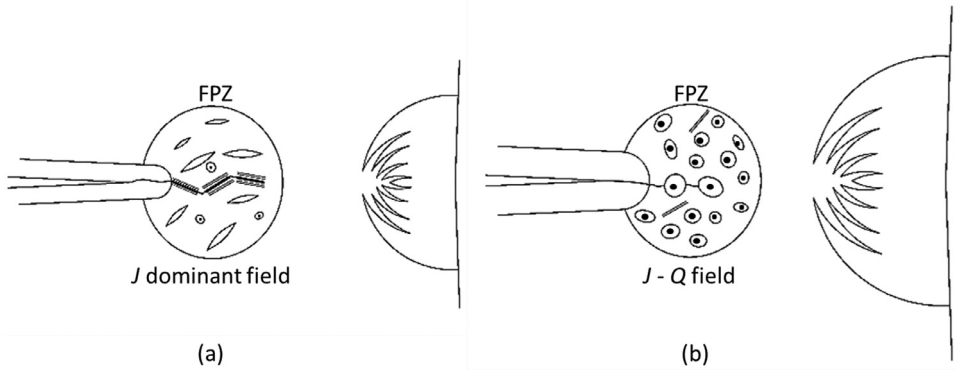

Fig. 14. Schematic representation of fracture process zone (FPZ) and far-field plastic region corresponding to (a) static test with high triaxiality near crack tip and (b) dynamic test with moderately reduced levels of triaxiality near crack tip.

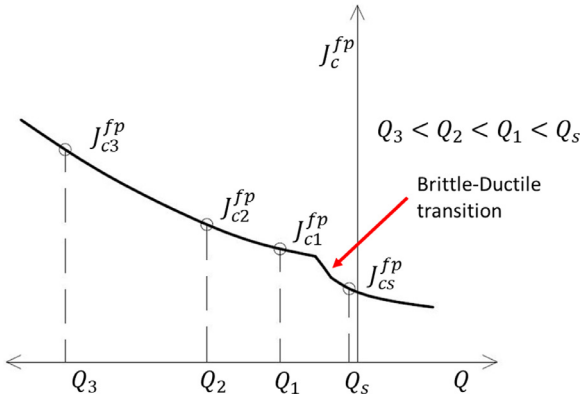

Fig. 15. Schematic showing variation of J_c^{fp} with crack tip constraint parameter Q. The specific values of J_c^{fp} for the static case ($Q = Q_s$) and those pertaining to increasingly negative Q levels (Q_1, Q_2, Q_3) attained with enhancement in $\dot{J}$ are indicated.

density of TTs near the specimen far-edge with many grains experiencing complete lattice re-orientation at high V_0 leading to pronounced texture changes (Fig. 13(c)). This corroborates well with the observation by Dudamell et al. [9] for AZ31 Mg alloy that under RD compression TT propagation is enhanced at high strain rates.

As suggested by Prasad et al. [14], the contribution from TTs to the background plastic dissipation in the ligament can be estimated as

$$U_{tw}^{p} = W_{tw}^{p} V_{tw}, \tag{4}$$

where, $W_{tw}^{p} = \tau_{tw}\gamma_{tw}$ is the specific plastic work due to tensile twinning and $V_{tw} = BA_{tw}\, f_{avg}$ is the volume of twinned region in the ligament. Here, τ_{tw} is the average CRSS for tensile twinning (which is assumed as 40 MPa in the following computation [14,58]) and γ_{tw} is the twinning shear which is 0.13 [59]. Also, A_{tw} is the total (in-plane) area of the region adjacent to the uncracked ligament where twinning is observed (semi-circular white region in Fig. 10(a), (b), which has a radius of about 6 mm), B is the specimen thickness and f_{avg} is the average twin volume fraction in this region.

To obtain approximate upper bounds to f_{avg}, EBSD maps on the specimen surface near the far-edge such as those shown in Fig. 13 were used to evaluate the twinned area fraction (see supplementary material). Assuming that these twins persist through the specimen thickness as noted in [13], f_{avg} is then estimated as 0.21, 0.32 and 0.64 for the static case and dynamic loading with $V_0 = 9$ and 17 m/s, respectively. Further, in view of Eq.(2), the contribution from tensile twinning in background plastic zone to the toughness can be written as $J_c^{bp,tw} = \eta U_{tw}^{p}/(Bb)$. On using the data indicated above, this is found to be about 12.5 N/mm for the static case and about 19 and 38 N/mm for the dynamic loading with $V_0 = 9$ and 17 m/s, respectively. These rough estimates range between 32 and 47% of the corresponding total J_c values given in Table 2 and are therefore substantial. More importantly, it must be noted that the contribution to the toughness from dissipation due to twinning in the region adjacent to the ligament increases by a factor of three as loading changes from static to dynamic with $V_0 = 17$ m/s.

Interestingly, the overall enhancement in toughness as loading changes from static to dynamic with $V_0 = 9$ m/s, by combining the above two approximate estimates for J_c^{fp} and $J_c^{bp,tw}$ is about 31 N/mm which is comparable to the actual value of 28 N/mm indicated in Table 1. This suggests that the analysis presented here provides a rational basis for interpreting the results.

5. Concluding remarks

Static and dynamic fracture experiments (corresponding to different loading rates) have been conducted in this work, using fatigue pre-cracked three-point bend specimens of a rolled AZ31 Mg alloy. The focus of the work has been on understanding how TTs influence the fracture behavior at high loading rates caused by impact (resulting in $\dot{J}$ greater than 0.5 GN/(ms)). The key observation is that while the density of TTs near the loading edge enhances strongly with loading rate causing the lattice in many grains to re-orient, thereby imparting pronounced texture changes, it decreases near the crack tip. The former, which is consistent with high strain rate compression experiments performed along RD [9], leads to strong texture hardening as well as to elevation in the saturation value of the bending moment on the ligament. More importantly, it enhances the contribution to the overall toughness due to dissipation in the background plastic zone (which is roughly estimated to be more than a factor of 3 for $V_0 = 17$ m/s as compared to static loading).

The decrease in TT area fraction near the tip on the other hand, is attributed to drop in stress triaxiality caused by local material inertia which has been shown in previous elastic-plastic computational studies [29–33] to enhance with $\dot{J}$. In fact, even for the lowest $\dot{J}$ of about 0.5 GN/(ms), this constraint loss ($|Q\sigma_0|$) is expected to be around $0.6\sigma_0$ [30], which is comparable to the drop in stress triaxiality with increase in notch root radius between the sharply grooved RN2 and moderately notched RN10 cylindrical specimens tested under static loading by Kondori and Benzerga [3]. This results in a quasi-brittle to ductile transition (as in [3]) when loading changes from static to dynamic (even for the lowest V_0 of 9 m/s) with the fracture morphology comprising of highly elongated grooves (having aspect ratio of about 6) for the former and nearly equi-axed dimples (having aspect ratio around 1.5) for the

latter which appear to be triggered by Mn-rich particles. The average dimple size increases with loading rate which is qualitatively similar to the influence of increasing the notch root radius in the static fracture experiments of [15] and is again attributed to reduction in triaxiality.

Perhaps the most significant observation of this work is the strong increase in fracture toughness J_c from 32 N/mm for static loading to 88 N/mm (by almost 200%) corresponding to the dynamic test with $V_0 = 20$ m/s. This enhancement, which is higher than that reported in many other engineering alloys, has been rationalized from elevation of both the intrinsic work of separation and the background plastic dissipation as V_0 increases. This should have important implications to fracture based design of engineering components (such as in automotive or aircraft applications) where possible impact loading may occur triggering dynamic fracture at stress concentrations.

Declaration of Competing Interest

The authors declare that they have no known competing financial interests or personal relationships that could have appeared to influence the work reported in this paper.

Acknowledgements

R.Narasimhan would like to gratefully acknowledge the Science and Engineering Research Board (Government of India) for financial support through the J.C.Bose Fellowship research grant. The authors would like to thank Professor G. Ravichandran for providing experimental facilities and Dr. Zev Lovinger for helping with the dynamic tests.

Supplementary materials

Supplementary material associated with this article can be found, in the online version, at doi:10.1016/j.actamat.2020.10.059.

References

[1] B.L. Mordike, T. Ebert, Magnesium Properties - applications - potential, Mater. Sci. Eng. A. 302 (2001) 37–45.
[2] H. Somekawa, K. Nakajima, A. Singh, T. Mukai, Ductile fracture mechanism in fine-grained magnesium alloy, Philos. Mag. Lett. 90 (2010) 831–839.
[3] B. Kondori, A.A. Benzerga, Effect of stress triaxiality on the flow and fracture of Mg alloy AZ31, Metall. Mater. Trans. A Phys. Metall. Mater. Sci. 45 (2014) 3292–3307.
[4] M.R. Barnett, Twinning and the ductility of magnesium alloys. Part I: "Tension" twins, Mater. Sci. Eng. A. 464 (2007) 1–7.
[5] S.R. Agnew, Ö. Duygulu, Plastic anisotropy and the role of non-basal slip in magnesium alloy AZ31B, Int. J. Plast. 21 (2005) 1161–1193.
[6] M. Knezevic, A. Levinson, R. Harris, R.K. Mishra, R.D. Doherty, S.R. Kalidindi, Deformation twinning in AZ31: influence on strain hardening and texture evolution, Acta Mater. 58 (2010) 6230–6242.
[7] A. Pandey, F. Kabirian, J.H. Hwang, S.H. Choi, A.S. Khan, Mechanical responses and deformation mechanisms of an AZ31 Mg alloy sheet under dynamic and simple shear deformations, Int. J. Plast. 68 (2015) 111–131.
[8] I. Ulacia, N.V. Dudamell, F. Gálvez, S. Yi, M.T. Pérez-Prado, I. Hurtado, Mechanical behavior and microstructural evolution of a Mg AZ31 sheet at dynamic strain rates, Acta Mater. 58 (2010) 2988–2998.
[9] N.V. Dudamell, I. Ulacia, F. Gálvez, S. Yi, J. Bohlen, D. Letzig, I. Hurtado, M.T. Pérez-Prado, Twinning and grain subdivision during dynamic deformation of a Mg AZ31 sheet alloy at room temperature, Acta Mater. 59 (2011) 6949–6962.
[10] M. Zhao, V. Kannan, K.T. Ramesh, The dynamic plasticity and dynamic failure of a magnesium alloy under multiaxial loading, Acta Mater 154 (2018) 124–136.
[11] H. Somekawa, T. Mukai, Effect of grain refinement on fracture toughness in extruded pure magnesium, Scr. Mater. 53 (2005) 1059–1064.
[12] H. Somekawa, A. Singh, T. Mukai, Fracture mechanism of a coarse-grained magnesium alloy during fracture toughness testing, Philos. Mag. Lett. 89 (2009) 2–10.
[13] V. Kaushik, R. Narasimhan, R.K. Mishra, Experimental study of fracture behavior of magnesium single crystals, Mater. Sci. Eng. A. 590 (2014) 174–185.
[14] N.S. Prasad, N. Naveen Kumar, R. Narasimhan, S. Suwas, Fracture behavior of magnesium alloys - Role of tensile twinning, Acta Mater. 94 (2015) 281–293.
[15] N.S. Prasad, R. Narasimhan, S. Suwas, Effect of notch acuity on the fracture behavior of AZ31 Mg alloy, Eng. Fract. Mech. 187 (2018) 241–261.
[16] B. Selvarajou, B. Kondori, A.A. Benzerga, S.P. Joshi, On plastic flow in notched hexagonal close packed single crystals, J. Mech. Phys. Solids. 94 (2016) 273–297.
[17] B. Selvarajou, S.P. Joshi, A.A. Benzerga, Three dimensional simulations of texture and triaxiality effects on the plasticity of magnesium alloys, Acta Mater. 127 (2017) 54–72.
[18] M.J. Nemcko, H. Qiao, P. Wu, D.S. Wilkinson, Effects of void fraction on void growth and linkage in commercially pure magnesium, Acta Mater. 113 (2016) 68–80.
[19] A.K. Ray, D.S. Wilkinson, The effect of microstructure on damage and fracture in AZ31B and ZEK100 magnesium alloys, Mater. Sci. Eng. A. 658 (2016) 33–41.
[20] K.V. Vaishakh, R. Narasimhan, K.U. Yazar, S. Suwas, Mixed-mode (I and II) fracture behavior of a basal-textured magnesium alloy, Acta Mater. 193 (2020) 99–114.
[21] N. Subrahmanya Prasad, R. Narasimhan, S. Suwas, Numerical simulations of cylindrical void growth in Mg single crystals, Int. J. Fract. 200 (2016) 159–183.
[22] B. Selvarajou, S.P. Joshi, A.A. Benzerga, Void growth and coalescence in hexagonal close packed crystals, J. Mech. Phys. Solids. 125 (2019) 198–224.
[23] M.F. Kanninen, P.E. O'Donoghue, Research challenges arising from current and potential applications of dynamic fracture mechanics to the integrity of engineering structures, Int. J. Solids Struct. 32 (1995) 2423–2445.
[24] M.L. Wilson, R.H. Hawley, J. Duffy, The effect of loading rate and temperature on fracture initiation in 1020 hot-rolled steel, Eng. Fract. Mech. 13 (1980) 371–385.
[25] L.S. Costin, J. Duffy, The effect of loading rate and temperature on the initiation of fracture in a mild, rate-sensitive steel, J. Eng. Mater. Technol. Trans. ASME. 101 (1979) 258–264.
[26] H. Couque, Effect of loading rate on the plane stress fracture toughness properties of an aluminum alloy, J. Phys. IV JP. 4 (1994) 1–6.
[27] A. Venkert, P.R. Guduru, G. Ravichandran, An investigation of dynamic failure in 2.3Ni-1.3Cr-0.17C steel, Metall, Mater. Trans. A Phys. Metall. Mater. Sci. 31 (2000) 1147–1154.
[28] D.M. Owen, S. Zhuang, A.J. Rosakis, G. Ravichandran, Experimental determination of dynamic crack initiation and propagation fracture toughness in thin aluminum sheets, Int. J. Fract. 90 (1998) 153–174.
[29] S. Basu, R. Narasimhan, A Numerical investigation of loss of crack tip constraint in a dynamically loaded ductile specimen, J. Mech. Phys. Solids. 48 (2000) 1967–1985.
[30] P. Biswas, R. Narasimhan, A numerical study of constraint effects on dynamic ductile crack initiation, Mech. Mater. 34 (2002) 577–592.
[31] K.R. Jayadevan, R. Narasimhan, T.S. Ramamurthy, B. Dattaguru, Constraint loss under dynamic loading in rate independent plastic solids, Int. J. Fract. 116 (2002) 141–160.
[32] P. Biswas, R. Narasimhan, A. Tewari, Influence of crack tip constraint on void growth in ductile FCC single crystals, Mater. Sci. Eng. A. 528 (2011) 823–831.
[33] K.R. Jayadevan, R. Narasimhan, T.S. Ramamurthy, B. Dattaguru, A numerical study of T-stress in dynamically loaded fracture specimens, Int. J. Solids Struct. 38 (2001) 4987–5005.
[34] N.P. O'Dowd, Applications of two parameter approaches in elastic-plastic fracture mechanics, Eng. Fract. Mech. 52 (1995) 445–465.
[35] T.L. Anderson, Fracture Mechanics Fundamentals and Applications, 3rd Ed., CRC Press, Florida, 2004.
[36] S. Basu, R. Narasimhan, A finite element study of the effects of material characteristics and crack tip constraint on dynamic ductile fracture initiation, J. Mech. Phys. Solids. 47 (1999) 325–350.
[37] X. Yu, L. Li, T. Li, D. Qin, S. Liu, Y. Li, Improvement on dynamic fracture properties of magnesium alloy AZ31B through equal channel angular pressing, Eng. Fract. Mech. 181 (2017) 87–100.
[38] M.A.M. Daud, N.Z. Nasir, A. Rivai, M.Z. Selamat, Dynamic fracture toughness of magnesium alloy under impact loading conditions, Procedia Eng 53 (2013) 639–644.
[39] T. Nakamura, C.F. Shih, L.B. Freund, Analysis of a dynamically loaded three–point-bend ductile fracture specimen, Eng. Fract. Mech. 25 (1986) 323–339.
[40] J.R. Rice, P.C. Paris, J.G. Merkle, Some Further Results of J-Integral Analysis and Estimates, ASTM Spec. Tech. Publ. 536 (1973) 231–245.
[41] A.S.T.M. E1820-01, Standard Test Method for Measurement of Fracture Toughness, Annual Book of ASTM Standards (2003) 1–46.
[42] D.R. Ireland, Critical Review of Instrumented Impact Testing, in: Int. Conf. Dyn. Fract, Toughness, London, 1976, pp. 47–62.
[43] J. Zhang, S.P. Joshi, Phenomenological crystal plasticity modeling and detailed micromechanical investigations of pure magnesium, J. Mech. Phys. Solids. 60 (2012) 945–972.
[44] D. Peirce, C.F. Shih, A. Needleman, A tangent modulus method for rate dependent solids, Comput. Struct. 18 (1984) 875–887.
[45] K.V. Vaishakh, N. Subrahmanya Prasad, R. Narasimhan, Numerical investigation of the origin of anomalous tensile twinning in magnesium alloys, J. Eng. Mater. Technol. Trans. ASME. 141 (2019) 1–15.
[46] G. Green, J.F. Knott, The Initiation and Propagation of Ductile Fracture in Low Strength Steels., J. Eng. Mater. Technol. 98 (1976) 37–46.
[47] C.F. Shih, Relationships between the J-integral and the crack opening displacement for stationary and extending cracks, J. Mech. Phys. Solids. 29 (1981) 305–326.

[48] J.W. Hutchinson, Fundamentals of the phenomenological theory of nonlinear fracture mechanics, J. Appl. Mech. Trans. ASME. 50 (1983) 1042–1051.
[49] R. Narasimhan, A.J. Rosakis, A finite element analysis of small-scale yielding near a stationary crack under plane stress, J. Mech. Phys. Solids. 36 (1988) 77–117.
[50] C. Gandhi, M.F. Ashby, Overview no. 5. Fracture-mechanism maps for materials which cleave: F.C.C., B.C.C. and H.C.P. metals and ceramics, Acta Metall 27 (1979) 1565–1602.
[51] A.S.T.M. E562-19, Standard Test Method for Determining Volume Fraction by Systematic Manual Point Count, Annual Book of ASTM Standards (2019) 1–7.
[52] L. Capolungo, I.J. Beyerlein, Nucleation and stability of twins in hcp metals, Phys. Rev. B - Condens. Matter Mater. Phys. 78 (2008) 1–19.
[53] A. Needleman, Effect of size on necking of dynamically loaded notched bars, Mech. Mater. 116 (2018) 180–188.
[54] J. Koplik, A. Needleman, Void growth and coalescence in porous plastic solids, Int. J. Solids Struct. 24 (1988) 835–853.
[55] J.R. Rice, M.A. Johnson, et al., The role of large crack tip geometry changes in plane strain fracture, in: MF Kaninen, et al. (Eds.), Inelast. Behav. Solids, Ed., McGraw-Hill series in material science and engineering, New York, 1970, pp. 641–672.
[56] J.C. Baird, B. Li, S. Yazdan Parast, S.J. Horstemeyer, L.G. Hector, P.T. Wang, M.F. Horstemeyer, Localized twin bands in sheet bending of a magnesium alloy, Scr. Mater. 67 (2012) 471–474.
[57] M.R. Barnett, Z. Keshavarz, A.G. Beer, D. Atwell, Influence of grain size on the compressive deformation of wrought Mg-3Al-1Zn, Acta Mater. 52 (2004) 5093–5103.
[58] J. Wang, J.M. Molina-aldareguía, J. Llorca, Effect of Al content on the critical resolved shear stress for twin nucleation and growth in Mg alloys, Acta Mater. 188 (2020) 215–227.
[59] W.F. Hosford, E.W. Kelley, Plane-Strain Compression of Magnesium and Magnesium Alloy Crystals, Trans. Metall. Soc. AIME. 242 (1968) 5–13.